ELSEVIER

Contents lists available at ScienceDirect

Scripta Materialia

journal homepage: www.journals.elsevier.com/scripta-materialia





Retained-austenite transformation precedes grain fragmentation in carbon-partitioned QP1180 steel

Liliana Romero Resendiz ^{a,b,c}, Muhammad Naeem ^{b,c,*}, Vicente Amigo ^d, Christina Reinhard ^{e,f}, Stefan Michalik ^g, Terence G. Langdon ^h, Yi Huang ^a

- a Department of Design and Engineering, Faculty of Science and Technology, Bournemouth University, Poole, Dorset BH12 5BB, UK
- ^b School of Metallurgy and Materials, University of Birmingham, Birmingham B15 2TT, UK
- ^c Interdisciplinary Research Center, Liaoning Academy of Materials, Shenyang 110167, China
- d Instituto de Tecnología de Materiales, Universitat Politècnica de València, Camino de Vera s/n, Valencia 46022, Spain
- ^e The University of Manchester at Harwell, Diamond Light Source, Didcot, Oxfordshire OX11 ODE, UK
- f The University of Manchester, Faculty of Science and Engineering, Oxford Road, Manchester M13 9PL, UK
- ^g Diamond Light Source, Harwell Science and Innovation Campus, Didcot, Oxfordshire OX11 0DE, UK
- h Departments of Aerospace & Mechanical Engineering and Materials Science, University of Southern California, Los Angeles, CA 90089-1453, USA

ARTICLE INFO

Keywords: Quench & partitioning steel High-pressure torsion Mechanical properties Phase transformations Synchrotron diffraction

ABSTRACT

Understanding the mechanistic interplay between phase transformation and grain fragmentation is critical for microstructural control in advanced structural steels subjected to severe shear. Here, we investigate the activation sequence of retained-austenite transformation and grain fragmentation along the radial strain gradient of a single QP1180 steel disk processed by high-pressure torsion. Synchrotron-based high-energy X-ray diffraction and microscopy reveal a pronounced austenite $(\gamma) \rightarrow$ martensite (α'/α) transformation that saturates at a critical equivalent von Mises strain $\bar{e}_T \sim 8.5$. Concomitantly, γ grain size decreases sharply up to \bar{e}_T , while γ peak broadening and microstructural analysis suggest limited grain fragmentation of austenite during transformation. These findings demonstrate that γ -phase reduction is primarily driven by phase transformation prior to the onset of defect-induced fragmentation. This mechanistic activation order and the critical strain \bar{e}_T provide key inputs for calibrating physics-based constitutive models and defining robust process windows for industrial forming operations and component design.

Quench and partitioning (QP) steels are increasingly deployed in automotive body-in-white and high-performance structural parts because they can reach tensile strengths above 1 GPa while retaining a formability that rivals the dual-phase grades [1,2]. This exceptional balance stems from the presence of a tailored fraction of carbon-enriched, mechanically stable retained austenite (γ) [3]. When QP steel is deformed, the γ -phase gradually transforms to martensite and provides a transformation-induced plasticity (TRIP) hardening that delays necking [4]. In QP steel, the microstructure is first quenched between the martensite start and finish temperatures to form a martensite + austenite mixture, then held isothermally ("partitioning step") so that carbon diffuses from supersaturated martensite into austenite under (constrained) para-equilibrium conditions while carbide precipitation is suppressed by Si/Al additions [5]. Carbon-partitioning from martensite to austenite stabilizes the austenite and expands its

lattice [2,5]. Because industrial work hardening and crash events impose intense, often non-uniform shear strains, the reliability of QP components ultimately depends on how the γ -phase withstands such extreme gradient deformation fields [6].

The TRIP effect and its synergy with other strengthening mechanisms including grain boundaries and solid solutions have been widely documented in QP steels [7–9]. Among these, TRIP and grain refinement require critical stresses. While the mechanical behavior of QP steels relies heavily on these mechanisms, the activation sequence, whether strain-induced TRIP precedes or follows grain refinement under severe shear, remains unclear, motivating the present study.

To conduct a reliable study on the activation of these strengthening mechanisms, a single sample with a position-dependent strain gradient is necessary to avoid chemical or microstructural heterogeneity errors. High-pressure torsion (HPT) of a disk offers a radial strain gradient

E-mail addresses: m.naeem@bham.ac.uk, naeem@lam.ln.cn (M. Naeem).

 $^{^{\}ast}$ Corresponding author.

L.R. Resendiz et al. Scripta Materialia 271 (2026) 117024

ranging from essentially zero at the disk center to sufficient strain severity at the perimeter to overpass the critical stress for TRIP and grain refinement. In practice, HPT simultaneously subjects a thin disk to a gigapascal-level hydrostatic pressure and a large shear, thereby fragmenting grains to the submicrometric or nanometer scale [10]. A single HPT sample can include these strain gradients as a function of the radial distance, while the center of the sample is considered as nearly undeformed [11]. Under strain, two mechanisms compete: (i) a progressive $\gamma{\to}\alpha'/\alpha$ martensitic transformation and (ii) a grain subdivision of the retained γ by dislocation cell formation [1]. Which mechanism initiates first, and whether the local shear strain threshold for transformation differs from that for fragmentation, remains unresolved, and yet the answer is pivotal for use in constitutive models that aim to predict strain hardening and plasticity in metastable steels processed or formed under severe shear.

Here we address this gap by analyzing a single QP1180 disk subjected to one full HPT turn. The radial equivalent strain spans $\overline{\varepsilon}=0$ to 21.3 within a single mechanical history, thereby providing the entire pathway from an undeformed core to an edge where γ -phase disappears. Collecting synchrotron high-energy X-ray diffraction (HE-XRD) data along a line from the sample center to its edge enabled to follow the martensitic transformation through intensity changes of individual Bragg reflections, and possible grain fragmentations through broadening of reflections. Complementary transmission electron microscopy (TEM) and electron backscatter diffraction (EBSD) provided defect observations, phase maps, and grain size. This combined and spatially resolved dataset offers a strain-graded progression of the γ-phase fragmentation versus martensitic transformation that cannot be captured by sequential rolling or tensile testing, where each strain step entails a new sample preparation and arising of a possible microstructural heterogeneity between different samples. The insights from this work will therefore supply a mechanistic basis for tuning metastable steel behavior via controlled pre-shear or modified partitioning schedules, and establishes HPT as a rapid, high-resolution test bed for sequencing metastable-phase events.

QP1180 steel sheets (2.7Mn, 1.7Si, 0.2C, balance of Fe in wt. %) of 2 mm thickness were obtained from Baosteel company (China). 1 turn of HPT was applied at room temperature on a sample with a diameter of 10 mm and a thickness of 0.85 mm (Fig. S1). A pressure of 6 GPa was applied during rotation under quasi-constrained conditions created by an anvil diameter of 10 mm and cavity depth of 0.25 mm [12]. The equivalent von Mises strain $(\overline{\varepsilon})$ at a given radial position, r, was calculated using the expression $\overline{\varepsilon} = \frac{2\pi N}{t} \frac{r}{\sqrt{3}}$, where N is the number of turns and t is the sample thickness [10]. The temperature rise during HPT has no significant impact on microstructural evolution due to its low value from 5 to 50 °C [13].

For microstructural characterization, the samples were subjected to standard metallographic methods, culminating in a mirror-like finish achieved by polishing with a $0.1~\mu m$ diamond solution followed by a $0.04~\mu m$ colloidal silica suspension on a vibratory table. The microstructure was studied by EBSD with a step size of 0.07 μm and data analysis was performed with AZtecCrystal software. Phase and strain evolution were tracked by synchrotron-based HE-XRD carried out at beamline I12-JEEP [14] at the Diamond Light Source (UK). The HE-XRD measurements were performed with an X-ray beam energy of 78.234 keV (wavelength = 0.15848 Å) and a beam size of 0.5 mm \times 0.5 mm. Data were collected along a line from the sample edge to the center at 0.5 mm intervals (Fig. S1). The diffraction data were collected in transmission geometry using a Pilatus 2 M CdTe detector positioned at 601.79 mm from the sample and an exposure time of 4 s was used. The DAWN software was used for full azimuthal integrations of the acquired 2D diffraction rings and for peak profile fitting with a pseudo-Voigt function [15]. A NIST CeO2 674b standard was measured under identical conditions for calibration. Microscopy and HE-XRD analyses were taken at the perpendicular plane to the torsion direction, i.e., parallel to

the applied high-pressure direction (Fig. S1). The austenite phase fractions were estimated from HE-XRD data by Rietveld refinement. Focused ion beam (FIB) lamellae were prepared using a Thermo Scientific Helios 5 CX dual-beam microscope. Local microstructural analysis was performed using bright-field (BF) and dark-field (DF) imaging, along with selected-area electron diffraction (SAED), conducted on a JEM-F200 TEM. Austenite phase was highlighted in DF mode using γ -specific (200) and (220) reflections. For statistical relevance, at least 5 random fields were analyzed per sample condition. Area fractions of austenite phase were quantified from grayscale DF micrographs using ImageJ software.

Fig. 1a displays the 1D integrated HE-XRD patterns recorded every 500 µm from the disc edge ($\overline{\epsilon} \sim 21.3$) to the nearly undeformed center $(\overline{\varepsilon} \sim 0)$. In the edge pattern, only martensite (α'/α) peaks are visible, whereas at the center, multiple γ -phase peaks are present, as shown by the diffraction rings in Fig. 1b. This confirms that the γ -peaks present at the center disappeared at the edge of the HPT-processed sample, indicating a complete $\gamma \rightarrow \alpha'/\alpha$ phase transformation. The normalized area under the peak, which is an indicator of the phase contents, is shown in Fig. 1c. It displays a fast decrement of γ-phase between 5000 and 3000 $\mu m~(0<~\overline{\epsilon}<8.5)$. However, after $~\overline{\epsilon}\sim8.5$, which may be considered as the critical strain for bulk phase transformation ($\bar{\epsilon}_T$), the γ -phase content decreases at a slower pace and finally disappears at $\overline{\varepsilon} \sim 21.3$ (edge). The pole figures for the austenite phase (Fig. S2) show a nearly random crystallographic orientation at both the lowest (center) and highest (edge) applied strains. This confirms that texture has a negligible influence on the normalized peak areas in Fig. 1c, as expected from the use of full azimuthal integration of the diffraction rings. Compared to conventional tensile testing where the phase transformation is distributed across the gauge length, here the hydrostatic pressure of the HPT processing suppresses fracture and allows the transformation to exhaust within a radial band of ~2 mm, thereby defining a unique transformation strain $\bar{\epsilon}_T \sim 8.5$ after which the austenite content remains nearly constant (Fig. 1c). The C-rich γ peaks, including the (200) γ , drops from the very first sampling interval (from center to 4500 µm location) and this confirms that chemical stabilization is overcome abruptly once a critical shear strain is reached. The (200) reflection is emphasized due to the high signal-to-noise ratio and minimal overlap with martensite peaks (Fig. 1a). The $\gamma \rightarrow \alpha'/\alpha$ trend is corroborated by consistent area loss of the other γ -phase reflections in Fig. 1c. The full width at half maximum (FWHM) behavior of selected γ -reflections is displayed in Fig. 1d. The FWHM reflects a convolution of crystal size and strain broadening [16]. Size broadening reports the domain size limited by grain boundaries and planar faults, whereas strain broadening arises from microstrain produced mainly by dislocation fields and intergranular stresses. The FWHM increases modestly with strain and therefore the grain fragmentation is modest (FWHM increases ≤0.02 Å) and delayed up to $\overline{\epsilon}_T \sim 8.5$ (3000 µm from edge), implying that the transformation overtakes grain refinement.

Fig. 2 tracks the peak position through d-spacing of (311) and $(200)\gamma$. The $(311)\gamma$ reflection provides a robust measure of the lattice parameter evolution (see Fig. S3), while the (200)y plane exhibits enhanced expansion due to its sensitivity to carbon partitioning. The (311) γ and (200) γ planes expand ~1.0 % and ~2.3 % towards the edge relative to the center. The strain-dependent response can be divided into three main stages: 1) a relatively slow change in d-spacing up to an $\bar{\varepsilon}$ of \sim 4, 2) a rapid increase in d-spacing between strains of \sim 4 to \sim 15, and 3) a saturation or asymptotic behavior beyond $\bar{\varepsilon} \sim 15$ (Fig. 2). The initial slow evolution (stage 1, $\bar{\epsilon}$ < 4) probably reflects an early elastic accommodation of strain and the onset of the $\gamma \rightarrow \alpha'/\alpha$ martensitic transformation. During this stage, the retained austenite remains structurally intact with limited sub-grain fragmentation, although dislocations are present, leading to a minimal lattice distortion. In stage 2 ($4 \le \overline{\epsilon} \le 15$), the more rapid increase in d-spacing may result from cumulative lattice strain as the retained austenite becomes increasingly stressed while the

L.R. Resendiz et al. Scripta Materialia 271 (2026) 117024

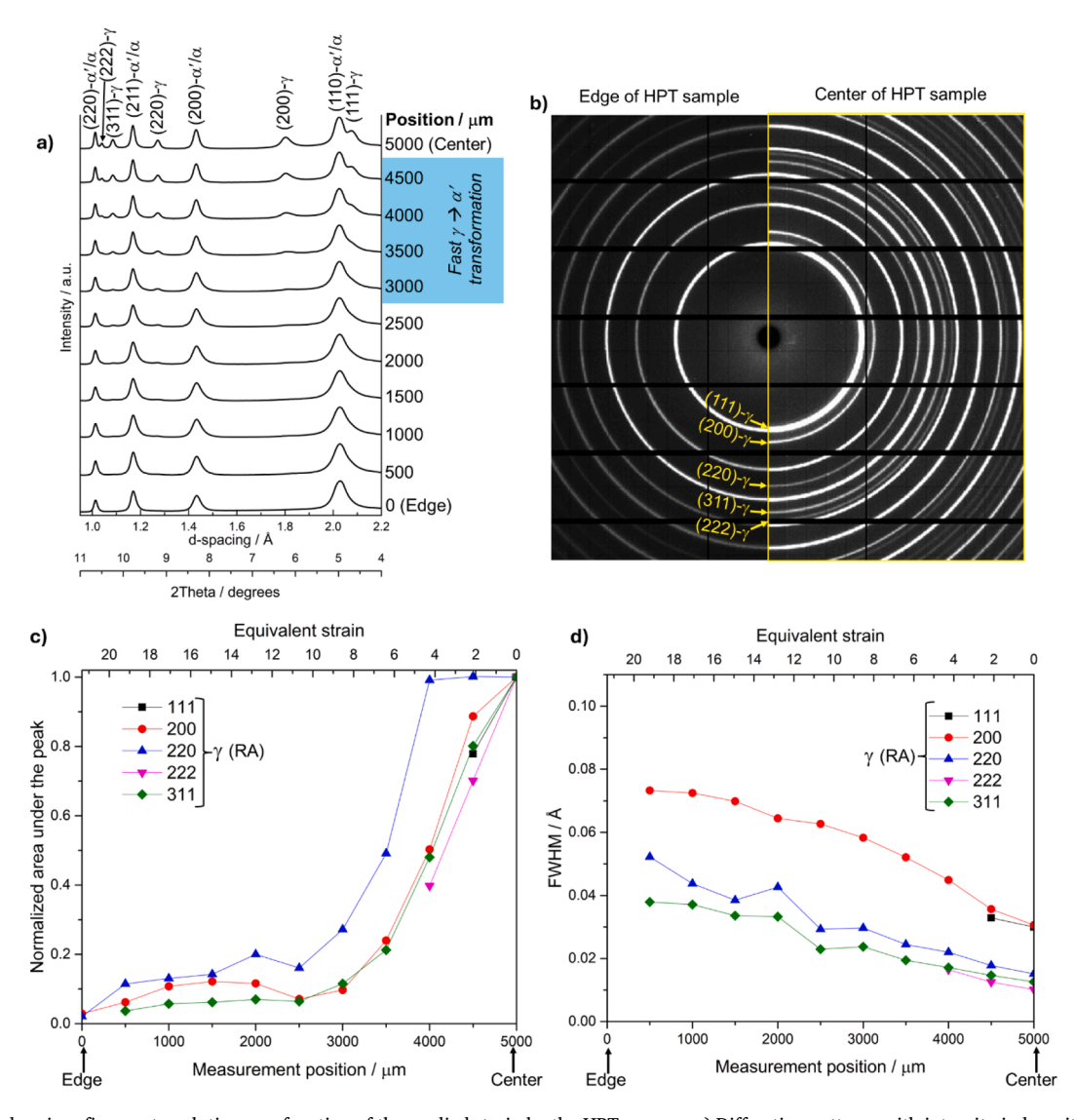


Fig. 1. Phase and grain refinement evolution as a function of the applied strain by the HPT process. a) Diffraction patterns with intensity in logarithm scale displays the $\gamma \rightarrow \alpha'/\alpha$ phase transformation detailed by the b) diffraction rings from the edge and center of the HPT sample with γ -peaks indexed. c) Normalized area under the γ -peaks, where decrement indicates a faster transformation up to an equivalent strain of $\sim 8.5~(\sim 3000~\mu m)$ from the edge of the HTP-processed sample. d) A continuous grain refinement is suggested by the semi-linear trend of FWHM with the applied strain.

martensitic transformation continues. Stage 3 ($\overline{\epsilon}$ >15), where the d-spacing becomes nearly constant despite increasing strain, indicates that a saturation point has been reached in terms of both elastic strain and phase contents. This plateau probably reflects the near-completion of the martensitic transformation in the high strain regions, leaving only highly stabilized retained austenite pockets or stress-shielded FCC grains which can no longer accommodate significant further elastic expansion. This observation is in good agreement with the plateau of austenitic peak areas at high strains shown in Fig. 1c. Importantly, the FCC peak shifts persist only if austenite remains elastically active [17].

Figs. 3 displays phase maps obtained by EBSD at $\overline{\epsilon} \sim 0$ (center), 8.5 (3000 µm from edge) and 21.3 (edge). The γ -phase content of 6.8 % at the central zone shows a fast decrement due to a strain-induced $\gamma \rightarrow \alpha'/\alpha$ phase transformation to 0.8 % at the intermediate location, finalizing with a slower reduction to 0.7 % at the edge. From the intermediate location to the edge, the residual γ -phase islands are <1 µm and often located at triple lines. There are no retained austenite stringers aligned with the shear direction, and this indicates that the transformation is not strain-partitioned into bands.

Despite the typical extensive grain refinement achieved by the severe plastic deformation processing, and especially for HPT which allows the $\,$

larger $\bar{\epsilon}$ [18], the γ -phase grain refinement is not major across the radius. The average γ -phase grain size decreases from 1.75 μm at $\bar{\epsilon} \sim 0$ to 0.21 μm at $\bar{\epsilon}_T \sim 8.5$ and does not fall significantly up to $\bar{\epsilon} \sim 21.3$ (0.14 μm). Grain size lags the significant change seen in Fig. 1, confirming that austenitic grain subdivision is not the rate-limiting step for the $\gamma \rightarrow \alpha'/\alpha$ reaction. The most plausible interpretation is that carbon-mediated instability, assisted by dislocation-enabled short-circuit diffusion, initiates the $\gamma \rightarrow \alpha'/\alpha$ transformation prior to extensive boundary-mediated fragmentation ($\epsilon^- \sim 8.5$), as indicated by the rapid loss of the γ -peak area relative to the gradual FWHM increase (Figs. 1c,d). Accelerated atomic diffusion facilitated by moving dislocations in metals undergoing plastic deformation has been widely reported since the mid-20th century [19].

TEM analysis supports the mechanism of dislocation-enabled short-circuit diffusion assisting carbon-mediated instability (Fig. 4). At the center ($\overline{\epsilon} \sim 0$) and at 3000 μm ($\overline{\epsilon}_T \sim 8.5$), DF imaging oriented along (200) γ reflection highlights retained austenite (Figs.4a,b) while the corresponding BF images show dense dislocation networks within the γ -phase adjacent to martensite (Figs.4 a.1, b.1. This indicates that rapid $\gamma \rightarrow \alpha'/\alpha$ transformation does not preclude high dislocation density in the

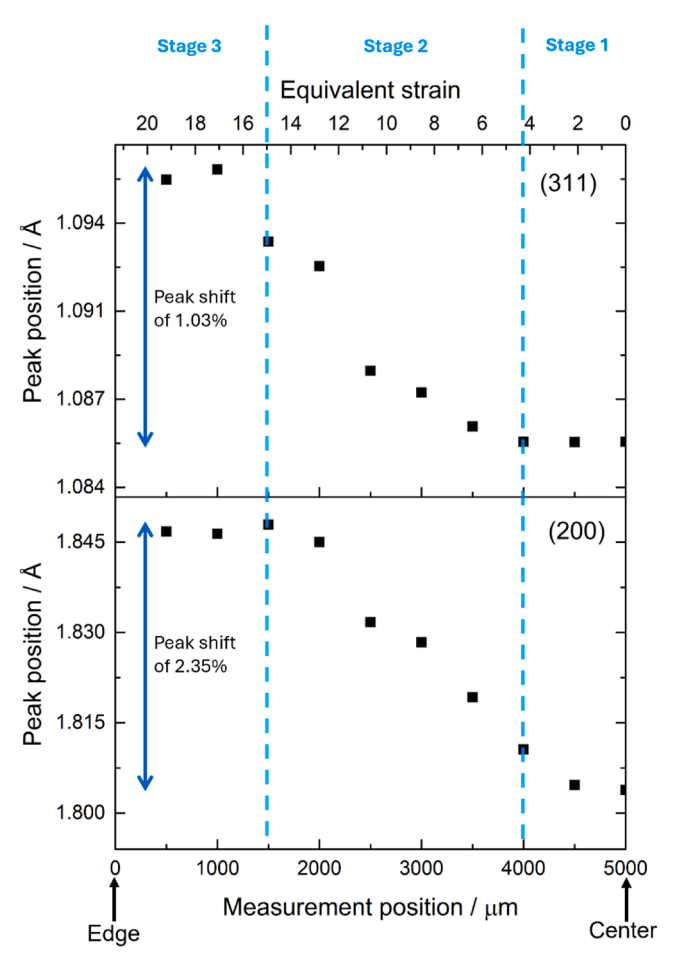


Fig. 2. Radial evolution of the retained-austenite lattice expansion expressed through the d-spacing of the $(311)\gamma$ and $(200)\gamma$ reflections. Each point represents the Bragg-peak maximum determined by pseudo-Voigt fit of the full Debye-Scherrer diffraction ring. Blue arrows highlight the total outward shift of the peaks between center and edge. The increase of d-spacing with strain for both reflections confirms a net lattice expansion of austenite prior to its disappearance, consistent with progressive carbon partitioning and/or hydrostatic-pressure relaxation.

residual γ-phase. The volume change and shape deformation associated with the $\gamma \rightarrow \alpha'$ transformation generate dislocations in the retained austenite to accommodate strain. These dislocations are stabilized by the constraints of the surrounding martensite, which suppresses their recovery and rearrangement into stable new grain boundaries (the essential step for fragmentation) during the rapid transformation process (Fig. 3). This is consistent with the modest FWHM increase compared to the steep decline of the γ -peak area up to $\overline{\varepsilon}_T$ (Fig. 1c,d). The coexistence of γ and α'/α is further confirmed by the indexed SAED patterns (Figs. 4 a.2–c.2). The dislocation networks within γ and their continuity across γ/α' interfaces provide short-circuit (pipe) diffusion paths for carbon, thereby accelerating the $\gamma \rightarrow \alpha'$ transformation [20]. After the transformation is exhausted, i.e., at the edge, DF image shows only sparse γ -phase films (Fig. 4c), while BF image (Fig. 4 c.1) indicates similar γ-phase domain size but increased defect contrast compared to those at lower strains.

Fig. 4d provides a cross-validation of the phase fractions using complementary techniques; EBSD and TEM resolve local heterogeneity whereas HE-XRD provides bulk statistics. All three methods show a steep drop in γ -phase from the center ($\overline{\epsilon} \sim 0$) to $\sim 3000~\mu m$ ($\overline{\epsilon} \sim 8.5$), followed by only a minor further decrease toward the edge ($\overline{\epsilon} \sim 21.3$). Therefore, this inter-method agreement substantiates accelerated $\gamma \rightarrow \alpha'/\alpha$ transformation before $\overline{\epsilon} \sim 8.5$. The three-stage evolution of (200) γ and (311) γ

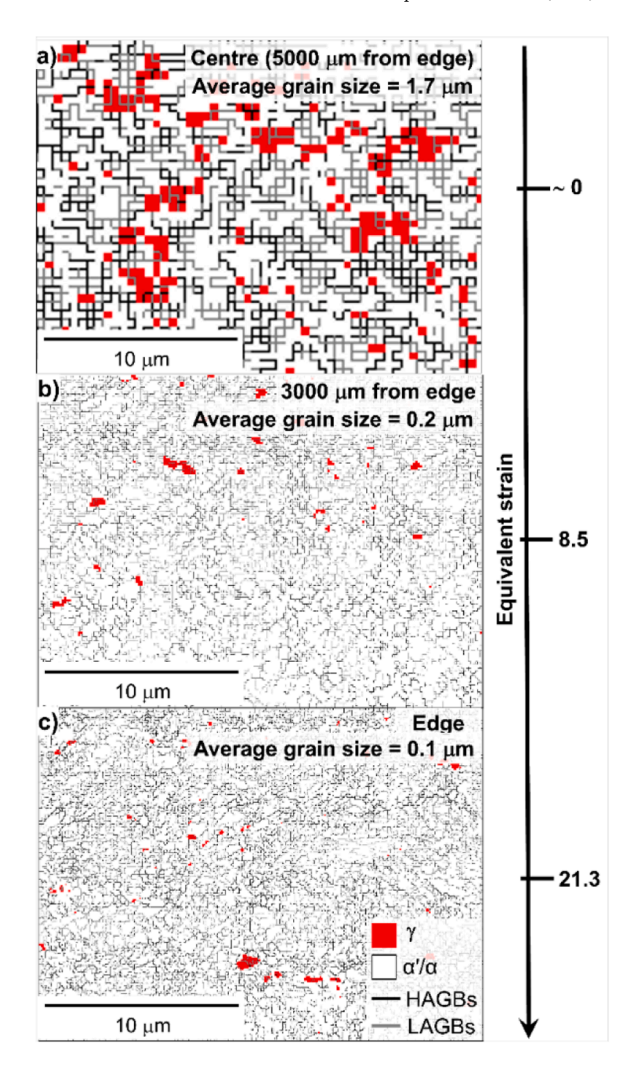


Fig. 3. Austenite phase and grain boundary mapping at a) center $(\epsilon^- \sim 0)$, b) ending position of faster $\gamma \rightarrow \alpha'/\alpha$ phase transformation, i.e., 3000 μ m from the edge $(\epsilon^- \sim 8.5)$, and c) edge $(\epsilon^- \sim 21.3)$, showing the decrement of retained-austenite as the equivalent strain increases.

d-spacings (Fig. 2) independently supports this interpretation.

Between 3000 µm and the edge, the γ -phase domain size in BF-TEM images (Figs. 4b.1,c.1) changes little, whereas the corresponding SAED patterns evolve from spottier arcs to more continuous rings with greater radial completeness. This evolution indicates an increase in diffraction-domain subdivision and microstrain, rather than a substantial change in the γ -phase grain size. This observation aligns with the HE-XRD data in Fig. 1, where the integrated γ -intensity remains nearly constant from $\overline{\epsilon} \sim 8.5$ to 21.3 while the FWHM increases. This combined evidence confirms that the microstrain accumulation and fragmentation dominate over further phase transformation in this high-strain regime.

Combining the HE-XRD, EBSD, and TEM evidence yields a coherent narrative: up to $\bar{\epsilon}_T$, the dislocation activity within γ (Figs.4 a.1,b.1) primarily triggers a fast phase transformation (Figs. 1c and 4d), while grain fragmentation proceeds slowly, as evidenced by the limited peak broadening (Fig. 1d). Between $\bar{\epsilon} \sim 7$ and 9, the local shear stress exceeds the mechanical and chemical barriers; carbon migrates from γ -phase into the high-density dislocation network of α'/α embryos and the γ peaks collapse although grain refinement remains incomplete. Fig. S4 shows a moderate FWHM increase in α'/α with strain, consistent with progressive defect accumulation and domain subdivision, which becomes faster when γ is near exhaustion. Beyond $\bar{\epsilon}_T \sim 8.5$, any residual γ is so sparse that its grain statistics and FWHM become unreliable and

L.R. Resendiz et al. Scripta Materialia 271 (2026) 117024

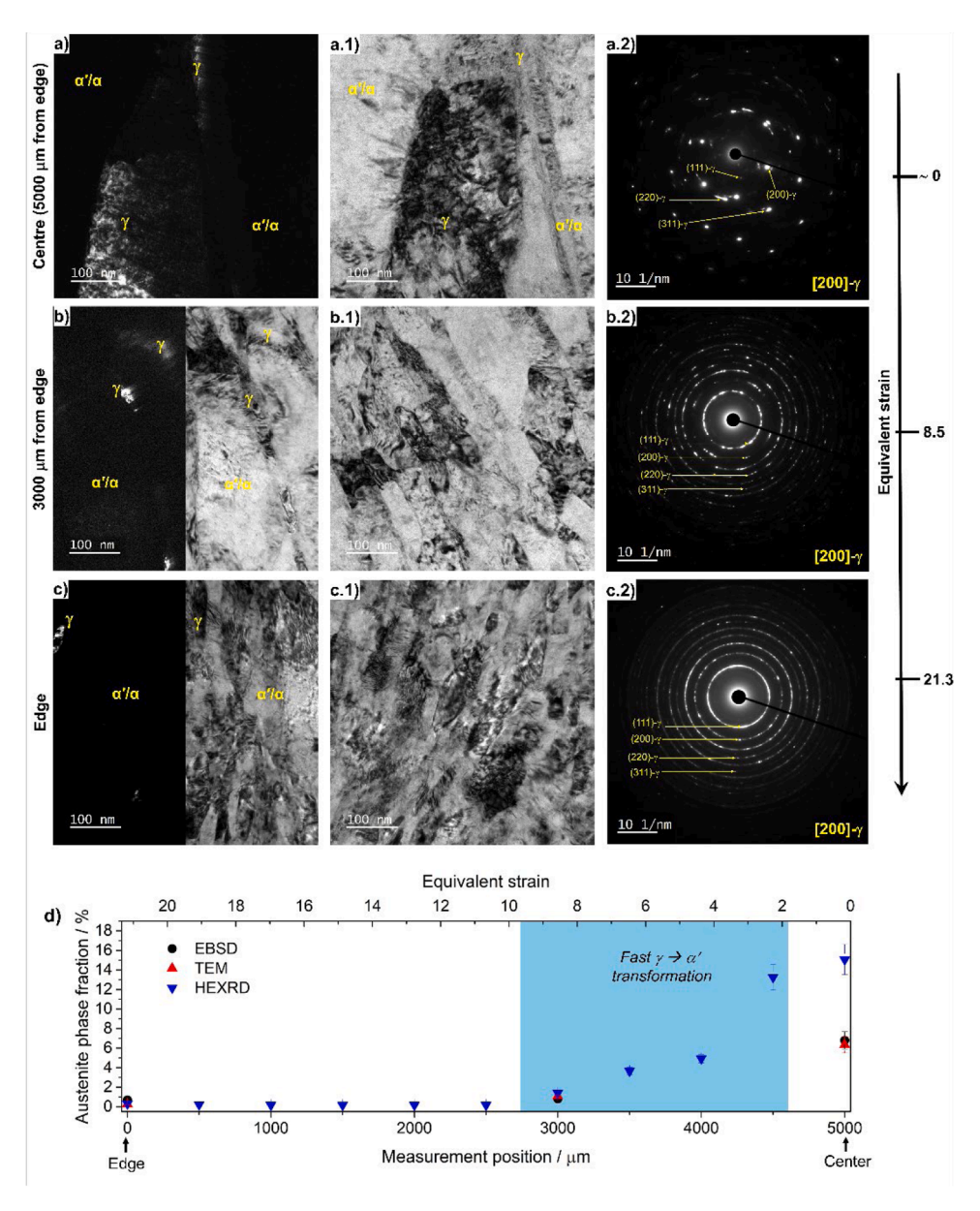


Fig. 4. TEM analysis of retained-austenite evolution along the HPT strain gradient at the a) center (5000 μm; $\bar{\epsilon}^-$ ~ 0), b) near-mid-radius (3000 μm; $\bar{\epsilon}_T$ ~ 8.5), and c) edge (0 μm; $\bar{\epsilon}^-$ ~ 21.3). a-c) phase-selective DF images using (200)γ reflection to highlight the γ-phase (bright) against the martensite α'/α (dark). a.1-c.1) BF images showing dense dislocation accumulation within the γ-phase compared to α'/α up to $\bar{\epsilon}_T$ ~ 8.5, as well as non-significant grain refinement after $\bar{\epsilon}_T$; a.2-c.2) SAED patterns with FCC peaks indexed confirming the presence of γ-phase. d) Austenite-phase fraction vs. radial position quantified by HE-XRD (bulk average), TEM (local 2D estimate), and EBSD (qualitative trend). The shaded region marks the interval where HE-XRD shows rapid exhaustion (ϵ^- ~ 7–9) of the $\gamma \rightarrow \alpha'/\alpha$ transformation, consistent with TEM and EBSD observations.

further strain is accommodated predominantly by α'/α . The HPT method thus decouples the two mechanisms and shows that TRIP precedes fragmentation in QP steels subjected to extreme shear.

The identification of \overline{e}_T provides a quantitative upper bound limit for QP sheet forming under severe shear conditions similar to HPT. It is important to note that this value is specific to the high-stress triaxiality of HPT; under lower stress triaxiality, the critical strain for transformation exhaustion will be lower. With this in mind, keeping local ε^- below 8 avoids premature TRIP exhaustion and preserves ductility. Conversely, pre-shearing to just beyond \overline{e}_T before crash-relevant loading could maximize the strength by exhausting γ -phase without requiring costly thermo-mechanical processing for nanocrystalline fragmentation. From a modelling viewpoint, the present data invite a two-step constitutive law in which carbon-mediated TRIP follows an Avrami-type kinetics triggered at \overline{e}_T , while dynamic Hall–Petch strengthening from

grain subdivision activates only after γ -phase is consumed. More broadly, the concept of a strain-threshold hierarchy, first a chemical-driven transformation and then microstructural refinement, may serve as a transferable design rule for other metastable FCC alloys (e.g., high-Mn TWIP or medium-Mn TRIP steels), thereby guiding process windows that either exploit or deliberately postpone TRIP to balance formability and final-part strength.

CRediT authorship contribution statement

Liliana Romero Resendiz: Writing – original draft, Methodology, Investigation, Funding acquisition, Formal analysis, Conceptualization. Muhammad Naeem: Writing – review & editing, Validation, Project administration, Methodology, Investigation, Conceptualization, Formal analysis. Vicente Amigo: Writing – review & editing, Resources,

Methodology. Christina Reinhard: Writing – review & editing, Methodology. Stefan Michalik: Writing – review & editing, Methodology. Terence G. Langdon: Writing – review & editing, Supervision, Conceptualization. Yi Huang: Writing – review & editing, Supervision, Resources, Project administration, Conceptualization.

Declaration of competing interest

The authors declare that they have no known competing financial interests or personal relationships that could have appeared to influence the work reported in this paper.

Acknowledgments

This work was supported by the HORIZON EUROPE programme of research and innovation of the European Union under the Marie Sklodowska-Curie Actions and financed by the UK Research and Innovation (EP/Y020545/1). The authors acknowledge Diamond Light Source for beamtime on I12-JEEP under proposal MG35888. The authors also thank Qin Zhang and Meng Chen for their assistance in preparing FIB lamellae and conducting TEM experiments, respectively.

Supplementary materials

Supplementary material associated with this article can be found, in the online version, at doi:10.1016/j.scriptamat.2025.117024.

References

- [1] S. Bai, Y. Chen, J. Sheng, D. Li, H. Lu, P. Bai, Z. Huang, J. Li, C. Zhao, A comprehensive overview of high strength and toughness steels for automobile based on QP process, J. Mater. Res. Technol. 27 (2023) 2216–2236, https://doi. org/10.1016/j.jimt.2023.09.210
- [2] M.J. Santofimia, L. Zhao, R. Petrov, C. Kwakernaak, W.G. Sloof, J. Sietsma, Microstructural development during the quenching and partitioning process in a newly designed low-carbon steel, Acta Mater 59 (2011) 6059–6068, https://doi. org/10.1016/j.actamat.2011.06.014.
- [4] D.V. Edmonds, K. He, F.C. Rizzo, B.C. De Cooman, D.K. Matlock, J.G. Speer, Quenching and partitioning martensite-A novel steel heat treatment, Mater. Sci. Eng. A 438–440 (2006) 25–34, https://doi.org/10.1016/j.msea.2006.02.133.
- [5] J. Speer, D.K. Matlock, B.C. De Cooman, J.G. Schroth, Carbon partitioning into austenite after martensite transformation, Acta Mater 51 (2003) 2611–2622, https://doi.org/10.1016/S1359-6454(03)00059-4.
- [6] O. Bouaziz, H. Zurob, M. Huang, Driving force and logic of development of advanced high strength steels for automotive applications, Steel Res. Int. 84 (2013) 937–947, https://doi.org/10.1002/srin.201200288.
- [7] L. Meng, W. Li, Q. Shi, H. Guo, W. Liang, H. Lu, Effect of partitioning treatment on the microstructure and properties of low-carbon ferritic stainless steel treated by a quenching and partitioning process, Mater. Sci. Eng. A 851 (2022) 143658, https://doi.org/10.1016/j.msea.2022.143658.

- [8] Y.Y. Cheng, G. Zhao, D.M. Xu, X.P. Mao, S.Q. Bao, G.W. Yang, Comparative study on microstructures and mechanical properties of Q&P steels prepared with hotrolled and cold-rolled C-Si-Mn sheets, J. Mater. Res. Technol. 20 (2022) 1226–1242, https://doi.org/10.1016/j.jmrt.2022.07.139.
- [9] S. Chu, W. Zhu, B. Mao, G. Hu, High strain rate deformation behavior of QP1180 advanced high-strength steel for automobiles, Mater. Sci. Eng. A 923 (2025) 147735, https://doi.org/10.1016/j.msea.2024.147735.
- [10] A.P. Zhilyaev, T.G. Langdon, Using high-pressure torsion for metal processing: fundamentals and applications, Prog. Mater. Sci. 53 (2008) 893–979, https://doi. org/10.1016/j.pmatsci.2008.03.002.
- [11] R.B. Figueiredo, M.T.P. Aguilar, P.R. Cetlin, T.G. Langdon, Analysis of plastic flow during high-pressure torsion, J. Mater. Sci. 47 (2012) 7807–7814, https://doi.org/ 10.1007/s10853-012-6506-z.
- [12] R.B. Figueiredo, P.H.R. Pereira, M.T.P. Aguilar, P.R. Cetlin, T.G. Langdon, Using finite element modeling to examine the temperature distribution in quasiconstrained high-pressure torsion, Acta Mater 60 (2012) 3190–3198, https://doi. org/10.1016/j.actamat.2012.02.027.
- [13] K. Edalati, Y. Hashiguchi, P.H.R. Pereira, Z. Horita, T.G. Langdon, Effect of temperature rise on microstructural evolution during high-pressure torsion, Mater. Sci. Eng. A 714 (2018) 167–171, https://doi.org/10.1016/j.msea.2017.12.095.
- [14] M. Drakopoulos, T. Connolley, C. Reinhard, R. Atwood, O. Magdysyuk, N. Vo, M. Hart, L. Connor, B. Humphreys, G. Howell, S. Davies, T. Hill, G. Wilkin, U. Pedersen, A. Foster, N. De Maio, M. Basham, F. Yuan, K. Wanelik, I12: the Joint Engineering, Environment and Processing (JEEP) beamline at Diamond Light Source, J. Synchrotron Radiat. 22 (2015) 828–838, https://doi.org/10.1107/ \$1600577515003513
- [15] J. Filik, A.W. Ashton, P.C.Y. Chang, P.A. Chater, S.J. Day, M. Drakopoulos, M. W. Gerring, M.L. Hart, O.V. Magdysyuk, S. Michalik, A. Smith, C.C. Tang, N. J. Terrill, M.T. Wharmby, H. Wilhelm, Processing two-dimensional X-ray diffraction and small-angle scattering data in DAWN 2, J. Appl. Crystallogr. 50 (2017) 959–966, https://doi.org/10.1107/S1600576717004708.
- [16] B.D. Cullity, Elements of X-Ray Diffraction, Addison-Wesley Metallurgy series, 1956.
- [17] M.T. Hutchings, P.J. Withers, T.M. Holden, T. Lorentzen, Interpretation and Analysis of Lattice Strain Data, Introduction to the Characterization of Residual Stress By Neutron Diffraction, Taylor & Francis Group, 2005.
- [18] K. Edalati, A.Q. Ahmed, S. Akrami, K. Ameyama, V. Aptukov, R.N. Asfandiyarov, M. Ashida, V. Astanin, A. Bachmaier, V. Beloshenko, E.V. Bobruk, K. Bryła, J. M. Cabrera, A.P. Carvalho, N.Q. Chinh, I.-C. Choi, R. Chulist, J.M. Cubero-Sesin, G. Davdian, M. Demirtas, S. Divinski, K. Durst, J. Dvorak, P. Edalati, S. Emura, N. A. Enikeev, G. Faraii, R.B. Figueiredo, R. Floriano, M. Fouladvind, D. Fruchart, M. Fuji, H. Fujiwara, M. Gaidics, D. Gheorghe, Ł. Gondek, J.E. González-Hernández, A. Gornakova, T. Grosdidier, J. Gubicza, D. Gunderov, L. He. O. F. Higuera, S. Hirosawa, A. Hohenwarter, Z. Horita, J. Horky, Y. Huang, J. Huot, Y. Ikoma, T. Ishihara, Y. Ivanisenko, J. Jang, A.M. Jorge, M. Kawabata-Ota, M. Kawasaki, T. Khelfa, J. Kobayashi, L. Kommel, A. Korneya, P. Kral, N. Kudriashova, S. Kuramoto, T.G. Langdon, D.-H. Lee, V.I. Levitas, C. Li, H.-W. Li, Y. Li, Z. Li, H.-J. Lin, K.-D. Liss, Y. Liu, D.M.M. Cardona, K. Matsuda, A. Mazilkin, Y. Mine, H. Miyamoto, S.-C. Moon, T. Müller, J.A. Muñoz, M.Yu. Murashkin, M. Naeem, M. Novelli, D. Olasz, R. Pippan, V.V. Popov, E.N. Popova, G. Purcek, P. de Rango, O. Renk, D. Retraint, Á. Révész, V. Roche, P. Rodriguez-Calvillo, L. Romero-Resendiz, X. Sauvage, T. Sawaguchi, H. Sena, H. Shahmir, X. Shi, V. Sklenicka, W. Skrotzki, N. Skryabina, F. Staab, B. Straumal, Z. Sun, M. Szczerba, Y. Takizawa, Y. Tang, R.Z. Valiev, A. Vozniak, A. Voznyak, B. Wang, J.T. Wang, G. Wilde, F. Zhang, M. Zhang, P. Zhang, J. Zhou, X. Zhu, Y.T. Zhu, Severe plastic deformation for producing superfunctional ultrafine-grained and heterostructured materials: an interdisciplinary review, J. Alloys Compd. 1002 (2024) 174667, https://doi.org/10.1016/j.jallcom.2024.174667
- [19] M. Cohen, Self-diffusion during plastic deformation, Transac. Japan Inst. Metal. 11 (1970) 145–151, https://doi.org/10.2320/matertrans1960.11.145.
- [20] G.R. Love, Dislocation pipe diffusion, Acta Metall. 12 (1964) 731–737. https://doi. org/10.1016/0001-6160(64)90220-2.